Structure, electric transport, and magneto-transport properties of metallic double-chain based $Pr_{1-x}Ca_xBa_2Cu_4O_8$ with low Ca substitution

Takehiro Teramura [a], Michiaki Matsukawa [a,*], Tatsuya Senzaki [a], Haruka Taniguchi [a], Kazuhiro Sano [b], Yoshiaki Ōno [c], Makoto Hagiwara [d]

[a] *Faculty of Science and Engineering, Iwate University, Morioka 020-8551, Japan*
[b] *Department of Physics Engineering, Mie University, Tsu 514-8507, Japan*
[c] *Department of Physics, Niigata University, Niigata 950-2181, Japan*
[d] *Kyoto Institute of Technology, Kyoto 606-8585, Japan*

ARTICLE INFO

ABSTRACT

In this study, we showed the crystal structure, electric resistivity, Seebeck and Hall coefficients, magneto-resistance, and magnetic susceptibility of $Pr_{1-x}Ca_xBa_2Cu_4O_8$ (x = 0.0, 0.02, and 0.05) are all relevant for our understanding of physical properties along CuO double chains. The lattice parameters of Ca substituted $PrBa_2Cu_4O_8$ remained almost invariant up to x = 0.05. Contrary to the Ca doping effect in the $PrBa_2Cu_3O_{7-\delta}$ system, the significant increases in the Seebeck and Hall coefficients due to the Ca substitution indicate a decrease in the carrier number. The significant magneto-resistance effect in the parent sample (16% at 10 K) was significantly reduced down to 5% in the x = 0.05 composition. On the basis of the two types of carrier models, we discussed the influence of Ca substitution on the electrical transport and magneto-transport properties.

1. Introduction

High-T_c cuprate materials have been widely studied from the different standpoints of science and engineering. Structurally, the Pr-based cuprates, $PrBa_2Cu_3O_{7-\delta}$ (Pr123) and $PrBa_2Cu_4O_8$ (Pr124), are identical to their corresponding Y-based high-T_c superconductors, $YBa_2Cu_3O_{7-\delta}$ (Y123) and $YBa_2Cu_4O_8$ (Y124). Pr123 and Pr124 compounds have insulating CuO_2 planes and are nonsuperconductive [1–3].

Pr124 system is a candidate material for a quasi one-dimensional (1D) metal. Pr124 compound has the CuO double-chains along the b-axis sandwiched between insulating CuO planes along the c-axis, as illustrated in Fig. 1(a). For Pr124 single crystals, it has been reported that the three-dimensional (3D) Fermi liquid state is realized at low temperatures due to small interchain hopping energies [4,5]. With increasing temperature, carrier hopping between chains is expected to become incoherent, resulting in a dimensional crossover from 3D Fermi liquid (FL) to 1D Tomonaga–Luttinger liquid (TLL) state [6]. However, the temperature-induced FL to TLL crossover predicted in the Pr124 system remains a controversial issue [7]. In the Pr124 system, it is challenging to control the oxygen stoichiometry because of its thermal stability in the oxidation atmosphere. Our motivation is to vary the carrier number along the CuO double chains due to the A-site partial

substitution of a divalent cation. There are numerous studies on the B-site substitution effect in $PrBa_2(Cu_{1-x}Zn_x)_4O_8$ to clarify the electronic state of CuO double chains so far [7,8]. The A-site substitution effect such as Ca^{2+} substitution for Pr^{3+} has not been investigated on structural and physical properties in the Pr124 system [9].

For $Pr_{1-x}Ca_xBa_2Cu_3O_{7-\delta}$ ($Pr_{1-x}Ca_x$123) thin films (x = 0.4 and 0.5), the partial substitution of Ca for Pr caused the hole doping in the CuO_2 plane and compensated for the suppression of superconductivity because of Pr ion [10,11]. Furthermore, Luszczek showed that hole doping is insufficient to compensate for suppressing superconductivity in the $Pr_{1-x}Ca_x$123 bulk ceramic samples. The Ca atoms introduced additional holes to the Pr123 system, but gave structural defects in the case of high Ca concentrations [12]. In the Pr123 structure, a systematic study on $PrBa_{2-y}Ca_yCu_3O_{7-\delta}$ (y = 0.1–0.4) showed that Ca ions can replace Pr ions but cannot substitute for Ba ions [13]. This result suggests that the ionic radius plays a more crucial role than the chemical properties since the ionic radius of Ca^{2+}(1.12 Å) is close to that of Pr^{3+} (1.126 Å)[14].

For its related Y124 system, Miyake reported that the partial substitution of Ca for Y increases a superconducting transition temperature (T_c), and $T_c \sim$ 90 K is achieved for $Y_{0.9}Ca_{0.1}Ba_2Cu_4O_8$ [15,16]. In $Y(Ba,Sr)_2Cu_4O_8$, there are recent studies on the stable improvement in

---

* Corresponding author.
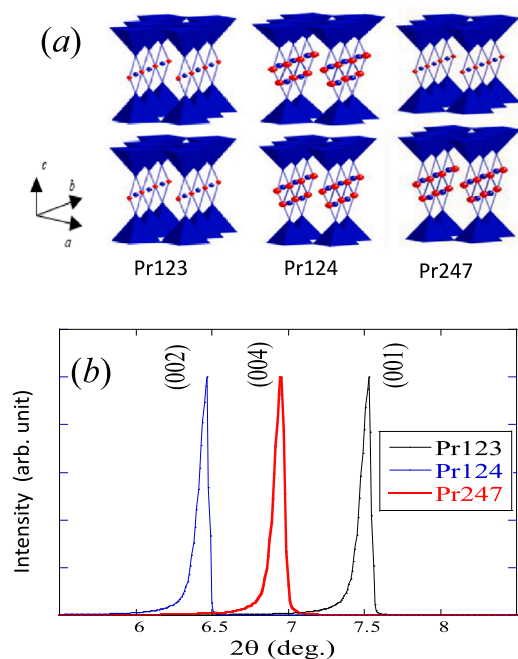 *E-mail address:* matsukawa@iwate-u.ac.jp (M. Matsukawa).

Fig. 1. (Color online) (*a*) Crystal structures of Pr123 with single-chain unit, Pr124 with double-chain unit, and Pr247 with single-chain and double-chain units alternately stacked along the *c*-axis. (*b*) Computed low-angle X-ray diffraction peaks showing the formation of Pr123, Pr124, and Pr247 phases. The indexed peak (002) in Pr124 is responsible for (001) in Pr123 because of the doubling of lattices along the *c*-axis. Similarly, the (004) peak in Pr247 corresponds to (002) in Pr124.

T_c up to 90 K because of the partial replacement of Sr^{2+} for Ba^{2+} [17, 18]. These results are related to the hole transfer from the CuO double chains to the CuO_2 planes by the chemical pressure effect due to the smaller Sr substitution.

A citrate pyrolysis approach is similar to nitrate combustion synthesis approaches [19,20] and a unique route to preparing reactive precursor mixtures through an ignition process of a concentrated aqueous solution including metallic ions of stoichiometric composition. For $YBa_2Cu_4O_8$ with $T_c = 80$ K and its related cuprate oxide compounds, high-quality single-phase polycrystalline materials are successfully synthesized under ambient pressure of oxygen gas at lower annealed temperatures [21–23]. We expect that this procedure allows us to prepare highly homogeneous and fine powders for functional oxide materials compared with conventional solid-state reaction approaches.

In this study, we try controlling the carrier number along the metallic CuO double chains through the partial substitution of Ca for the Pr site in the Pr124 system. Despite Ca^{2+} replacement for Pr^{3+}, our overall data suggest a significant reduction in the carrier number, which is in contrast with the Ca doping effect in the Pr123 system. The experimental outline is described in the next section. In Section 3, we show the experimental data, including the X-ray diffraction pattern, the electrical resistivity, the Seebeck and Hall coefficients, the magneto-resistance effect, and the magnetic susceptibility. Particularly, the X-ray data show that the Ca ion is incorporated into the crystal structure. For our understanding of a carrier suppression due to the Ca substitution, we discuss the transport properties of PrCa124 based on the two-types of carrier models.

2. Experiment

Polycrystalline samples of $Pr_{1-x}Ca_xBa_2Cu_4O_8$ (PrCa124) with $x = 0.0$, 0.02, and 0.05 were synthesized using the citrate pyrolysis approach. In the first step, at 70 °C–80 °C, stoichiometric mixtures of high purity Pr_6O_{11}, $CaCO_3$, $Ba(NO_3)_2$, and CuO were dissolved in nitric

acid solution. After adding citric acid and neutralizing it with aqueous ammonia, we obtained the porous products through the self-ignition process using halogen-lamp stirrer. (Molar ratio of metal cations, citric acid, and nitric acid, PrCa124: $C_6H_8O_7$: $HNO_3 = 1:6:10$) In the next step, the precursors were ground and the resultant fine powders were annealed under ambient oxygen pressure at 860 °C–891 °C for an extended period over 110–120 h using three zones controlled electric furnace to attain higher homogeneous temperature gradient.

For the scanning electron microscope (SEM) measurement, polycrystalline films on Ag substrates were fabricated using an electrophoretic deposition approach, to show the microstructures of PrCa124 single-phase samples. The sample powders were suspended in an acetone and iodine bath and the electrophoretic deposition was performed in the bath under the application of an electric voltage of up to 100 V for 60–100 s, [23,24]. We set the Pt and Ag plates as anode and cathode, respectively.

We conducted X-ray diffraction measurements on the produced samples at room temperature using an Ultima IV diffractometer (Rigaku) employing Cu-Kα radiation. The lattice parameters were estimated from the X-ray diffraction data employing the least-squares fits. The composition was analyzed using an electron probe micro analyzer (EPMA, JEOL). For the Ca substituted samples, we obtained $Pr_{0.972}Ca_{0.027}Ba_{2.10}Cu_{3.81}O_{8.18}$ at $x = 0.02$ and $Pr_{0.944}Ca_{0.055}Ba_{2.13}Cu_{4.08}O_{7.94}$ at $x = 0.05$.

Typical dimensions of the pelletized rectangular sample were $4.2 \times 3.4 \times 1.0$ mm^3. The electrical resistivity in a zero magnetic field was measured using the *dc* four-terminal method. The magneto-transport up to 9 *T* was measured by the *ac* four-probe method using a physical property measuring system (PPMS, Quantum Design), elevating temperatures from 5 K to 40 K. The applied magnetic field was perpendicular to the applied electric current's direction. The Seebeck coefficient (S) was determined from thermal voltages along the measured sample's longitudinal direction [25] with a temperature difference of a few Kelvins. Chromel-constantan thermocouples were used for measuring probes. The absolute values of S were calibrated using a reference material of high purity Pb rod. The Hall coefficient measurement at room temperature was performed with the five-probe technique using the PPMS, sweeping the applied field from +6 to −6 T. We measured the temperature variation of the *dc* magnetization under zero-field cooling (ZFC) process of 0.1 *T* employing a superconducting quantum interference device magnetometer (MPMS, Quantum Design).

3. Results and discussion

3.1. Synthesis and structure

Chemical synthesis, including citrate pyrolysis preparation, ensures the homogeneity, compared with conventional solid-state reaction synthesis. Furthermore, chemical synthesis can produce very fine powders. All starting materials were dissolved in HNO_3 to obtain nitrate mixtures. The citric acid ($C_6H_8O_7$) was added to nitrate mixtures as a chelating agent and appropriate amounts of aqueous ammonia (NH_3) were added to adjust the pH value to ~6.9. After neutralizing the mixture solution, the metal citrate complexes with stoichiometric composition and its associated ammonium nitrate (NH_4NO_3) were formed. NH_4NO_3 was employed for facilitating the auto-combustion process.

The addition of excess ammonia over the neutralization probably yields metal ammine complexes, instead of metal citrate complexes. We expect that the excess ammonia prevents chelating respective metal ions with $C_6H_8O_7$(complexant) and violates compositional homogeneity among the constituents, resulting in non-stoichiometric precursors. Similarly, for spinel ferrite synthesis, the pH = 7 was adapted in Ref. [20]. Finally, spontaneous combustion reactions occurred due to NH_4NO_3 through heating the resultant precursors using a halogen-lamp type hot plate. (refer to a video file recording the typical combustion process, which will be given as supplementary data in Appendix A.) For

Table 1

Structural properties of $Pr_{1-x}Ca_xBa_2Cu_4O_8$ (x = 0.0, 0.02, and 0.05). The typical lattice parameters are estimated from the experimental results in Fig. 4.

Ca content x	Annealing temp. (°C)	Orthorhombic phase (space group)	a (Å)	b (Å)	c (Å)
0.0	891	Pr247(Ammm)	3.8925	3.9100	50.793
0.0	860	Pr124(Ammm)	3.8850	3.9004	27.261
0.02	860	Pr124(Ammm)	3.8823	3.9019	27.276
0.05	880	Pr123(Pmmm)	3.8710	3.9297	11.727
0.05	860	Pr124(Ammm)	3.8840	3.8988	27.293

(a) x=0

(b) x=0.05

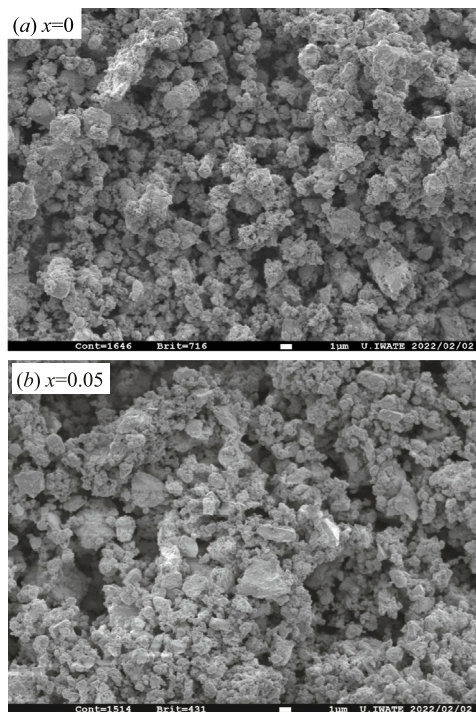**Fig. 2.** (Color online) SEM images of $Pr_{1-x}Ca_xBa_2Cu_4O_8$ polycrystalline films fabricated from single phase powders prepared by the citrate pyrolysis . (a) x = 0.0 and (b) 0.05.

the SEM measurement, polycrystalline films on Ag substrates were prepared from the PrCa124 powders using an electrophoretic deposition approach. The SEM images of Fig. 2 showed that the polycrystalline grains with a few micron sizes are homogeneously dispersed.

As shown in Fig. 1(a), we show the crystal structures of Pr123 with a single-chain unit, Pr124 with a double-chain unit, and Pr247 with single-chain and double-chain units alternately stacked along the c-axis. Additionally, the computed low-angle X-ray diffraction curves (Fig. 1(b)) are made clear, to identify their existing phases with the formation of Pr123, Pr124, and Pr247. Furthermore, we computed the main and satellite peaks for Pr123, Pr124, and Pr247 near 2θ = 30–35 °C using the published data (Fig. 3(a)–(c)).

Next, Fig. 4 shows X-ray diffraction patterns of Ca substituted polycrystalline samples as a function of oxygen annealing temperature between 860 °C and 891 °C ((a) x = 0.0, (b) x = 0.02, and (c) x = 0.05). For the parent samples, the Pr124 phase was stably formed within all annealing temperature ranges, except for the Pr247 phase prepared at a high temperature of 891 °C. For both the Ca2% and Ca5% substituted samples, the Pr124 phase was established at lower annealing temperatures, while the Pr123 phase was formed at higher temperatures. The X-ray diffraction curves for Pr123, Pr124, and Pr247 were computed using the corresponding lattice parameters, which will be given in Table 1 and Fig. 5. Additionally, for Ca5% substituted compounds, the Pr123 and Pr124 phases were formed at the

annealing temperature regions of 880 °C–891 °C, and 860 °C–868 °C, respectively, as shown in X-ray diffraction patterns of Fig. 4 (c). Near the intermediate annealing temperature of 873 °C, the Pr123 phase was primarily detected accompanied by a minority phase of Pr124, as evidenced from the magnified data in the inset of the lower panel on the left-hand side (Fig. 4 (c)). For instance, we noticed three satellite peaks of Pr124 near 30° and identified one low-angle peak around 6.5° with (002) index of Pr124. It was hard to separate the main peaks of the Pr123 and Pr124 phases from the observed data since they were completely overlapped near 30°.

In Fig. 3(d), we show the enlarged X-ray data around 30° for the Ca5% samples were annealed at 880 °C, which agrees well with the computed patterns of the $BaCuO_2$ cubic phase. Judging from their measured intensities, we give a rough estimation of several weigh percentages for the impurity phase. In the case of light Ca substitution, we detected no impurity phase of calcium oxides such as Ca_2CuO_2 besides $BaCuO_2$.

Now, we plot, in Fig. 5(a), (b), and (c), the lattice parameters as a function of annealing temperature for the x = 0.0, x = 0.02 and x = 0.05 samples, respectively. Here, the lattice parameters were estimated from the X-ray diffraction data employing the least-squares fits. These values are in fair agreement with the published data [30–32] for the Pr124, Pr247, and Pr123 compounds. The gray areas represent the stable formation of the Pr124 phase. The Ca substitution at Pr sites suppresses the phase boundary between Pr124 and Pr123 (or Pr247) down to the lower temperature side. For the YCa124 system, it has been reported that the synthesis boundary between the Y124 and Y123 phases shifts the lower annealing temperatures with increasing Ca content [33]. However, the lattice parameters of the Ca substituted Pr124 (or Pr123) remain nearly constant compared with these values of the Ca-free parent samples. This result is probably related to the fact that the ionic radius of Ca^{2+}(1.12 Å) is close to that of Pr^{3+} (1.126 Å), as mentioned in Ref. [13]. For the Ca lightly substituted $Y_{1-x}Ca_xBa_2Cu_4O_8$ (x = 0.0, 0.05, and 0.1) system, it has been reported that upon increasing the Ca content, the c-axis slightly elongates but both the a and b-axes remain unchanged [15]. For the oxygen concentration in $PrBa_2Cu_3O_{7-\delta}$, we evaluate from the lattice parameters in Fig. 5 that $7 - \delta$ is around 6.9, which is located around the optimal region [32]. From the EPMA analysis, the oxygen contents of the Ca substituted Pr124 samples are about the nominal value as mentioned before.

3.2. Resistivity and Seebeck coefficient

Next, we analyzed the effect of Ca substitution on the electrical transport properties of Pr124. In Fig. 6(a), the electrical resistivities for $Pr_{1-x}Ca_xBa_2Cu_4O_8$ (x = 0.0, 0.02, and 0.05) are shown as a function of temperature. With increasing the Ca content, the electrical resistivities gradually increased over various temperatures accompanied by suppression in a maximum peak temperature from 190 K at x = 0.0 down to 138 K at x = 0.05. Despite Ca^{2+} replacement for Pr^{3+}, the increased resistivity data for PrCa124 imply a decrease in the carrier number. Inset of Fig. 6 (a) shows ρ vs. T for the Ca 5% substituted samples annealed under three different conditions. A Ca 5% substituted sample annealed at 880 °C (Pr123 phase) showed a semiconducting behavior like pure Pr123. However, ρ of the x = 0.05 sample annealed at 873 °C
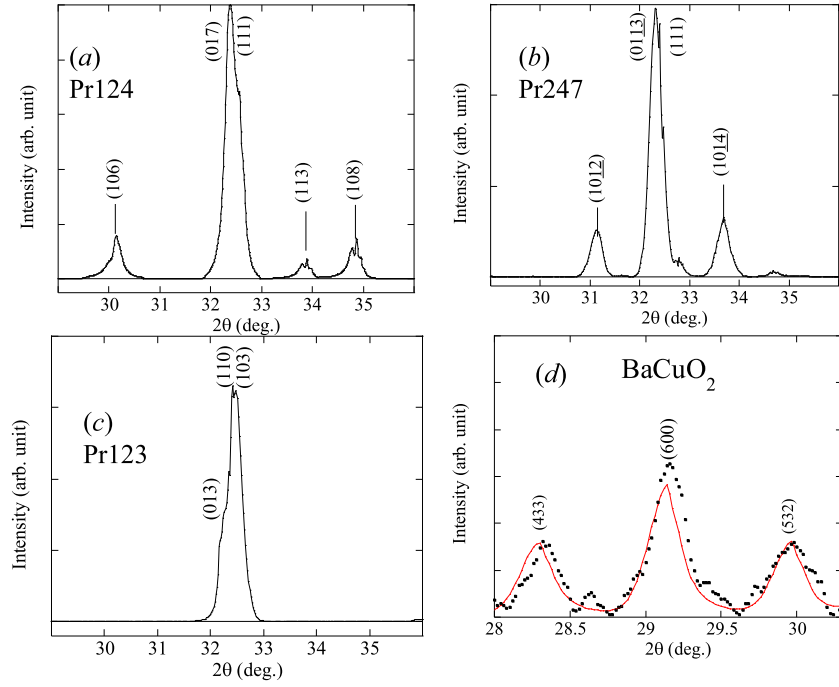
Fig. 3. (Color online) Calculated X-ray diffraction patterns of Pr124 (*a*), Pr247 (*b*), and Pr123 (*c*) near $2\theta = 30°–35°$. (*d*) Enlarged X-ray data around 30° for the Ca5% samples annealed at 880 °C. They are well fitted by the simulated curve of the BaCuO$_2$ cubic phase.

Table 2
Physical properties of $Pr_{1-x}Ca_xBa_2Cu_4O_8$ (x = 0.0, 0.02, and 0.05). The typical data are collected from the experimental results in Figs. 6–8.

Ca content x	ρ (300 K) (mΩcm)	$\Delta\rho/\rho$ (10 K) (%)	S (290 K) (μV/K)	R_H (270 K, 300 K) (10^{-3} cm^3/C)	μ_{eff} (μ_B)
0.0	2.1	16	20	1.2, 1.1	3.07
0.02	2.8	–	26		
0.05	3.1	5	29	1.9, 1.6	2.95
0.0[26]	1.2	16	27	–, 0.4[a]	3.11[c]
(Pr$_{1-x}$Ca$_x$123)					
0.0 [12]	~400	–	93	–, 6.7[b]	
0.1 [12]	~80	–	77		

[a]Ref. [27]
[b]Ref. [28]
[c]Ref. [29]

was strongly suppressed and it followed a metallic property at lower temperatures below ~100 K. As mentioned in Section 3.1, the x = 0.05 sample annealed at 873 °C contained the Pr124 minority phase with metallic properties, which contributes to a substantial decrease in the low-temperature resistivity.

Fig. 6 (*b*) illustrates Seebeck coefficients (S) as a function of temperature for $Pr_{1-x}Ca_xBa_2Cu_4O_8$ (x = 0.0, 0.02, and 0.05). For the parent and Ca substituted samples, the values of S at high temperatures were improved due to Ca substitution. In the 1D electron correlated system, such as a quasi 1D organic conductor, the Seebeck coefficient is well described by the Heikes formula $S = (k_B/e)\ln[2(1-x)/x]$ (x:carrier concentration) at high temperature limit [34,35]. Following the simple model, S shows a monotonous increase with decreasing the hole concentration from x = 0.5, indicating that larger magnitudes of S offer lower carrier contents. In a conventional metal, the Seebeck coefficient is given in such a way,

$$S(T) = \frac{(\pi k_B)^2 T}{3e} \left\{ \frac{1}{N(E)} \frac{dN(E)}{dE} \right\} \qquad (1)$$

where $N(E)$ represents the density of electronic state (DOS). In our previous study [36], we computed the energy derivative of the DOS as a function of the electron density using density functional band

calculation, assuming the energy dispersion $E(k)$ of the CuO double-chain model proposed by Habaguchi et al. [37]. These results provide $(1/N)(dN/dE) > 0$ for the hole-doped region ($n > 0.5$). An increase in the hole number (decreasing the electron number from 1) yields a decrease in $(1/N)(dN/dE)$ reducing S in Eq. (1). Thus, the improvement of S due to Ca substitution also suggests a decrease in the carrier number along the CuO double chains. Furthermore, the temperature variation of S for the parent sample showed a quick decrease from ~200 K and then reached quite a small value (~1μV/K) at lower temperatures below 100 K. Particularly, the latter behavior has a deep relationship with crossover from 1D to 2D in the low-temperature electronic states, as mentioned by Terasaki [26]. In the 2D electron system, it has been well accepted that the density of states becomes a constant. Therefore, assuming that Seebeck coefficient is proportional to the energy derivative of DOS, then S approaches a zero value. This trend was a common future for all samples studied.

The magnetic field dependence of the Hall voltage for the x = 0.0 and 0.05 samples at 270 K is plotted in the inset of Fig. 6 (*b*). Applying a linear fit to the Hall data, we obtained the Hall coefficient (R_H) for the x = 0.0 and 0.05 samples, as listed in Table 2. The Ca substitution at Pr site affected R_H at 270 K from 1.2×10^{-3} cm^3/C at the x = 0.0 sample to 1.9×10^{-3} cm^3/C at the x = 0.05 sample. This finding suggests
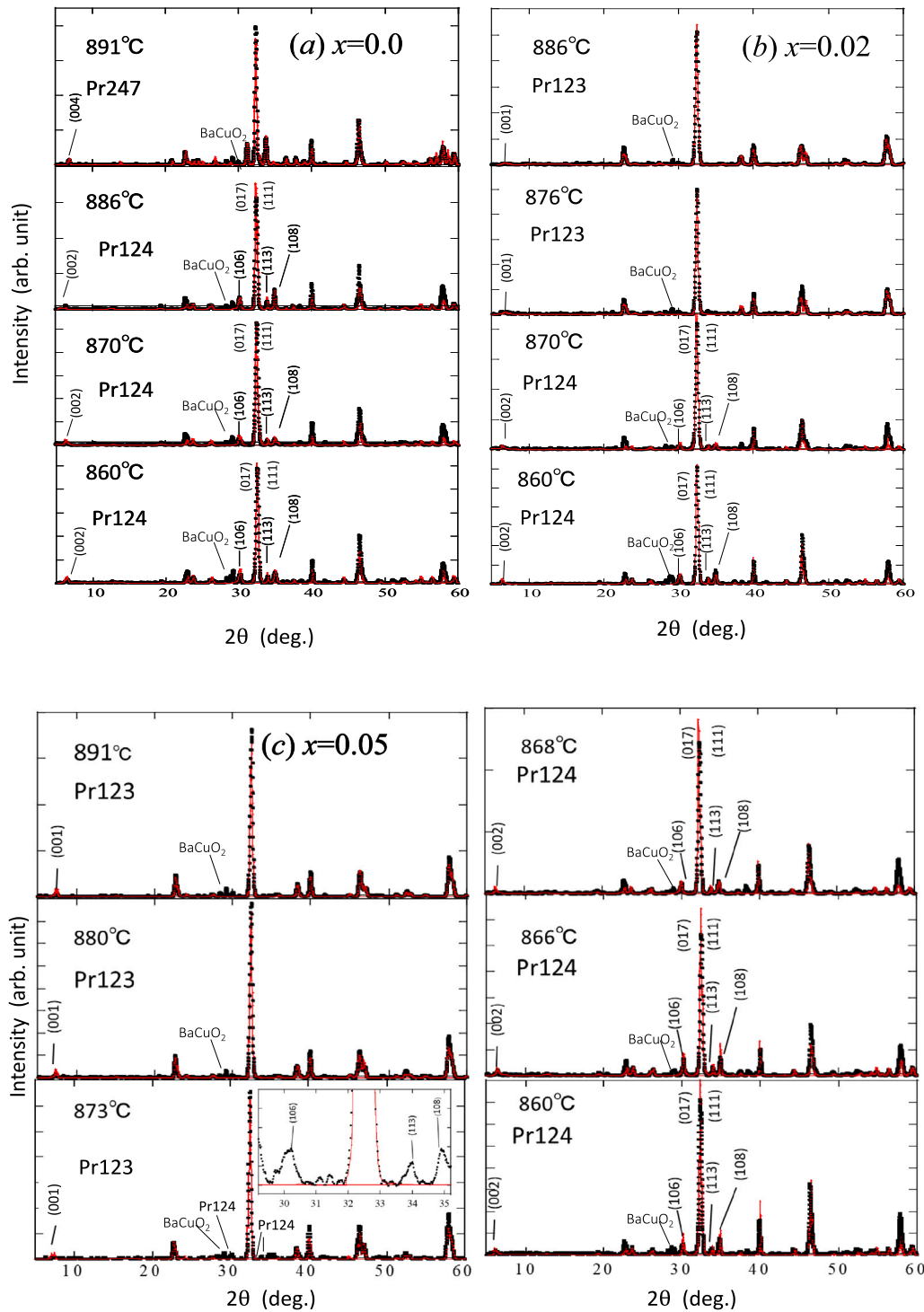
Fig. 4. (Color online) X-ray diffraction patterns of polycrystalline samples as a function of oxygen annealing temperature (860~891 °C). (*a*) *x* = 0.0, (*b*) *x* = 0.02 and (*c*) *x* = 0.05. The X-ray diffraction curves for Pr123, Pr124, and Pr247 were computed using the corresponding lattice parameters, which will be given in Table 1 and Fig. 5. For the parent samples, the Pr124 phase was stable except for Pr247 phase formed at 891 °C. For both Ca2% and Ca5% substituted samples, the Pr124 phase was established at lower annealing temperatures, while the Pr123 phase was formed at higher temperatures.

a substantial drop in carrier density due to the Ca substitution, which is almost consistent with the enhancement of the Seebeck coefficient at higher Ca content. For comparison, the published data for the Pr123 system are cited in Table 2. The Ca substitution at the Pr site suppressed both the electrical resistivity and the Seebeck coefficient through hole doping in the CuO_2 plane of the Pr123 phase. However, the effect of Ca substitution in the Pr124 system caused a significant increase in both ρ

and S accompanied by a drop in the carrier density. Thus, considering the main conduction channel along the CuO double chains in the Pr124 phase, the suppression in the carrier number is probably attributed to CuO double-chain block.
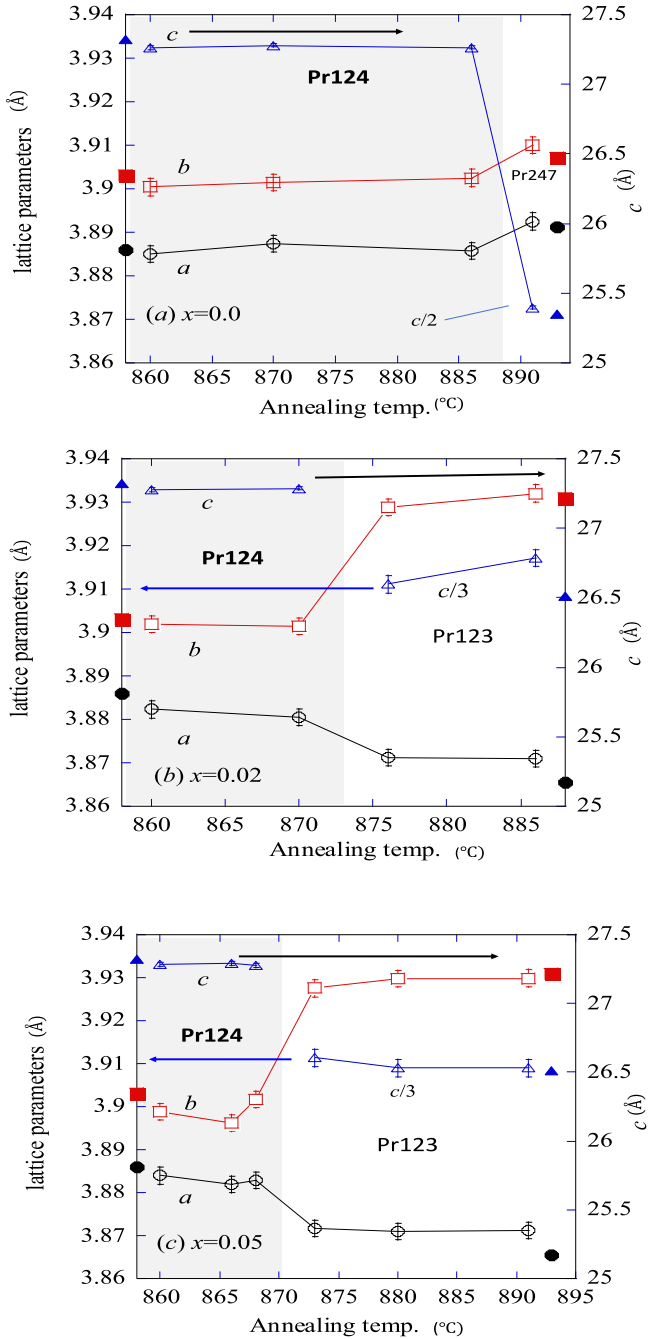
Fig. 5. (Color online) Lattice parameters vs annealing temperature. (a) $x = 0.0$, (b) $x = 0.02$ and (c) $x = 0.05$. The gray areas represent the stable formation of the Pr124 phase. The closed symbols (●: a-axis, ■: b-axis, ▲: c-axis) represent the published data [30–32]. (Pr124:Horii, Pr247:Yamada, Pr123:Lopez-Morales).

3.3. Magneto-resistance

Additionally, we demonstrated magneto-resistance (MR) effect, $\Delta\rho/\rho(0) = (\rho(H)-\rho(0T))/\rho(0T)$, measured at selected temperatures for $Pr_{1-x}Ca_xBa_2Cu_4O_8$ ($x = 0.0$ and 0.05) (Fig. 7). First, the MR data were almost fitted by H^2 solid curves. In Ref. [26], the low-temperature positive MR effect in Pr124 is explained by the classical model, in which electron orbitals are distorted by Lorentz force in the 2D electronic state. Secondly, a large MR effect observed in the parent sample (∼16% at 10 K) was strongly suppressed down to ∼5% in the Ca $x = 0.05$ substituted case. This suppression in the MR effect will be
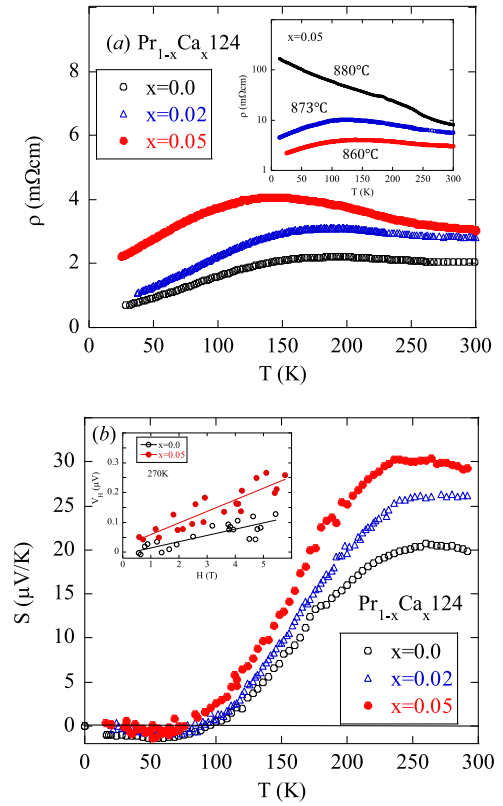

Fig. 6. (Color online) Temperature dependences of electrical resistivities and Seebeck coefficients, (a) and (b), for $Pr_{1-x}Ca_xBa_2Cu_4O_8$ ($x = 0.0$, 0.02, and 0.05). Inset of (a) shows ρ vs. T for the Ca 5% substituted samples annealed under three different conditions. Magnetic field dependence of the Hall voltage for the $x = 0.0$ and 0.05 samples at 270 K is plotted in the inset of (b). Applying a linear fit to the Hall data gives rise to Hall coefficient (R_H) for the $x = 0.0$ and 0.05 samples as listed in Table 2.

discussed later in terms of the two types of carries model. We give some comments on the magneto-resistance effect of disordered Pr124 single crystals using Kohler's plot. Narduzzo measured the b-axis magneto-resistance data for Pr124 crystals with different levels of disorder and examined their MR behavior using Kohler's plot [38]. For disordered samples, it was revealed that the positive MR effect is more enhanced accompanied by deviations from Kohler's rule. The suppressed MR data for PrCa124 are in contrast to those for the disordered Pr124 crystals. In Fig. 7(c), we plotted MR data at selected temperatures as a function of $(H/\rho(0))^2$. For both the Ca0% and Ca5% samples, we understand that Kohler's plots follow no single curve at temperature region above 15 K, indicating violation of Kohler's rule. Our MR data for the Ca5% substituted sample is not explained by the same scenario as the anomalously enhanced MR in Pr124 single crystals. In the initial fields, the weakly negative MR effect appeared for both the $x = 0.0$ and 0.05 samples, which seems to be related to a suppression of carrier scattering by Pr 4f spin. The low-temperature magnetization data were measured under ZFC of 0.1 T for both the $x = 0$ and 0.05 samples, as illustrated in the inset of Fig. 8. The antiferromagnetic transition temperature $T_N = 17$ K of the $x = 0$ sample remains constant due to the Ca substitution, resulting in a similar trend in the low field negative MR effect. Applying the Curie–Weiss law to the magnetic susceptibility data illustrated in Fig. 8, we evaluated the magnetic moment $\mu_{eff} = 3.07$ μ_B at Ca0% and 2.95 μ_B at Ca5%. The value decreased by about 4% due to the Ca5% substitution. The magnitude of the magnetic moment for the Ca5% substituted sample is reduced by 5% because the nonmagnetic ion of Ca^{2+} is partially replaced with the Pr^{3+} ion. This experimental estimation is not so far from the suggested value. The estimated value (3.07 μ_B) is smaller than the magnetic moment of
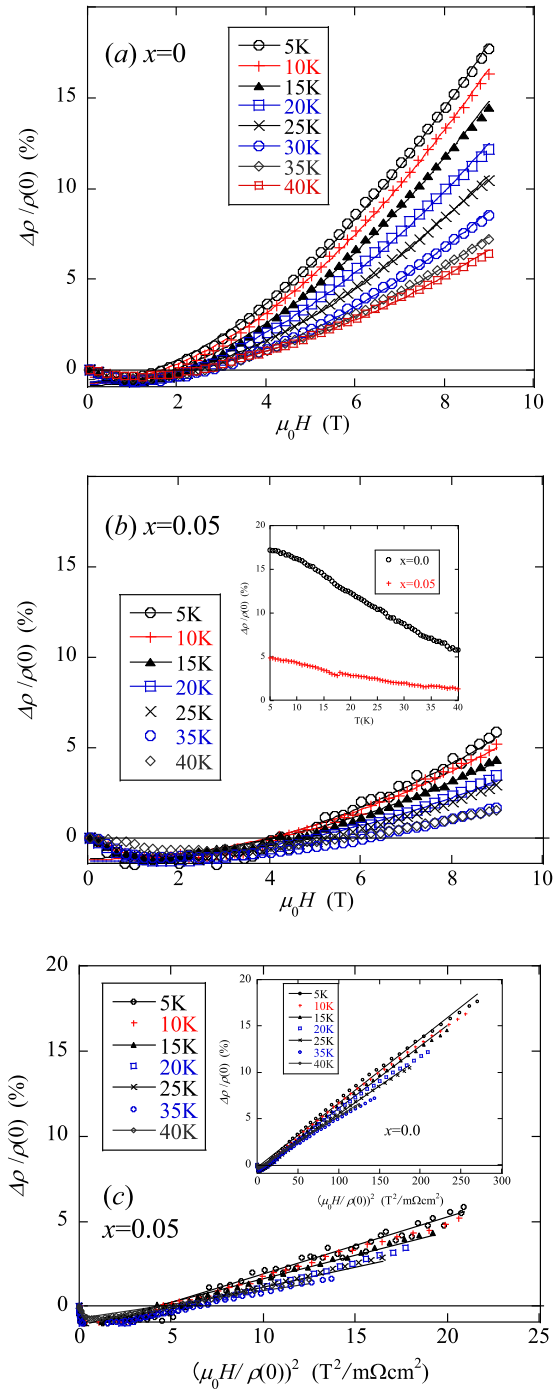
Fig. 7. (Color online) Magneto-resistance effect, $\Delta\rho/\rho(0) = (\rho(H)-\rho(0T))/\rho(0T)$, at selected temperatures, (a) $x = 0.0$ and (b) $x = 0.05$, for $Pr_{1-x}Ca_xBa_2Cu_4O_8$. MR data beyond 2T are almost fitted by H^2 solid curves. Inset of (b) shows $\Delta\rho/\rho(0) = (\rho(9T)-\rho(0T))/\rho(0T)$, as a function of temperature for both compositions. In (c) $x = 0.05$, we plotted MR data at selected temperatures as a function of $(H/\rho(0))^2$. Inset of (c) shows Kohler's plot for the parent sample.

the Pr^{3+} free ion (3.58 μ_B), which is closely related to the crystal field effect or hybridization effect of Pr-4f and O-2p orbitals [28].

Finally, we discuss our high-temperature experimental data for the Seebeck and Hall coefficients, applying the two types of carrier models with electrons and holes [39]. First, the total conductivity is written as the sum of electron and hole components
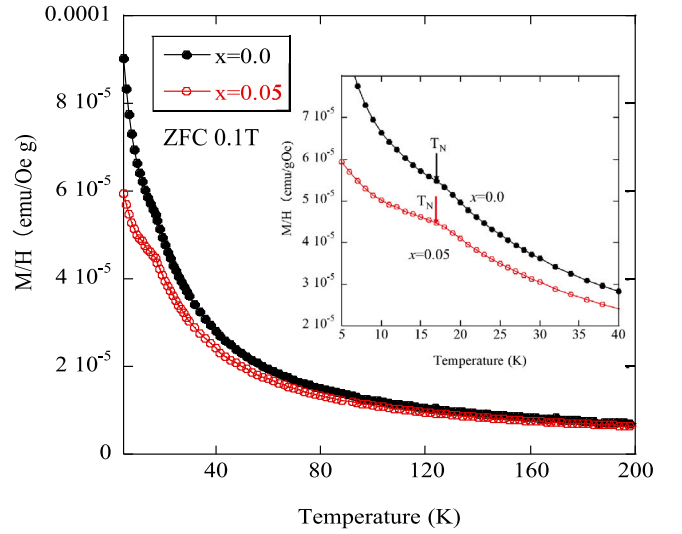
$$\sigma = \sigma_1 + \sigma_2 = n_1 e\mu_1 + n_2 e\mu_2$$

Fig. 8. (Color online) Temperature dependence of magnetic susceptibility measured under ZFC of 0.1 T for both the $x = 0.0$ and 0.05 samples. The arrows in the inset represent the antiferromagnetic transition temperature $T_N = 17$ K.

where σ_i, n_i, and μ_i (i=1 and 2: electron and hole) represent the conductivity, the carrier number and the mobility, respectively. Thus, the total Seebeck coefficient is expressed using the electron and hole conductivities, σ_1 and σ_2 [40],

$$S = \frac{\sigma_1 S_1 + \sigma_2 S_2}{\sigma_1 + \sigma_2} \quad (2)$$

where S_1 (< 0) and S_2 (> 0) are responsible for the electron and hole components, respectively. Additionally, the Hall coefficient for the two types of carrier models is given by the following formula,

$$R_H = \frac{\mu_2^2 n_2 - \mu_1^2 n_1}{e(n_1\mu_1 + n_2\mu_2)^2}$$

Here, we assume that the number of electron carriers is smaller than that of hole carriers, $n_1 < n_2$, keeping the electron and hole mobilities such as $\mu_1 \sim \mu_2$. However, we set the number of electron carrier n_1 to be zero and that of hole carrier n_2 to be constant. For clarification, we represent the corresponding conductivity, Seebeck coefficient, and Hall coefficient as σ', S', and R'_H, respectively. For the former and latter transport coefficients, we have $\sigma > \sigma'$, $S < S'$, and $R_H < R'_H$ as follows,

$$\sigma = e\mu_2(n_1 + n_2) > \sigma' = n_2 e\mu_2$$

$$S = \frac{n_1 S_1 + n_2 S_2}{n_1 + n_2} < S' = S_2 \ (S_1 < 0, S_2 > 0)$$

and

$$R_H = \frac{n_2 - n_1}{e(n_1 + n_2)^2} < R'_H = 1/en_2.$$

These rough estimations qualitatively reproduce the high-temperature improvements for the resistivity, the Seebeck coefficient, and the Hall coefficient due to Ca substitution. We note that a significant decrease in the electron density after the Ca substitution at the Pr site is an essential assumption.

Furthermore, we give some comments on the effect of magneto-resistance for $Pr_{1-x}Ca_x124$ ($x = 0.0$ and 0.05). According to the transport coefficient classical theory, we obtain the magneto-resistance formula at small magnetic fields H,

$$\Delta\rho/\rho(0) = \frac{\sigma_1\sigma_2(\beta_1 + \beta_2)^2 H^2}{(\sigma_1 + \sigma_2)^2} \quad (\beta_i = e\tau_i/m_i) \quad (3)$$

where τ_i and m_i represent the relaxation time and effective mass for the corresponding carrier ($i = 1$ and 2: electron and hole). Generally,

the existence of magneto-resistance in metal is evidence for different types of carriers [39]. When the two types of carriers such as different masses or different charges are deflected by different amounts in the magnetic field, it is impossible to find an electric field that will keep both components of the current going in the same direction. The given formula (3) for the two types of carrier models supports that $\Delta\rho$ is proportional to H^2. Furthermore, if the electrons are removed ($n_1 \sim 0$), we then obtain that $\Delta\rho \sim 0$. This simple estimation is consistent with the suppressed MR effect for the Ca substituted sample. If we assume that the electron carriers are removed because of the Ca substitution, our overall experimental results are well explained on the basis of the two types of carrier transport classical model.

In conclusion, we tried controlling the carrier number along the metallic CuO double chains through the partial substitution of Ca for the Pr site in the Pr124 system. The Pr/Ca124 compounds with low Ca substitution were successfully synthesized using the citrate pyrolysis approach. The lattice parameters remained almost constant for the Ca content, and the Ca ion was incorporated into the crystal structure. Despite the addition of a divalent ion, our overall data suggest a significant reduction in the carrier number, which is in contrast with the Ca doping effect in the Pr123 system. We discussed the influence of Ca substitution on the electrical transport and magneto-transport properties based on the two types of carrier model.

CRediT authorship contribution statement

Takehiro Teramura: Investigation, Writing – original draft, Investigation. **Michiaki Matsukawa:** Writing – review & editing, Investigation. **Tatsuya Senzaki:** Investigation. **Haruka Taniguchi:** Investigation. **Kazuhiro Sano:** Investigation. **Yoshiaki Ōno:** Investigation. **Makoto Hagiwara:** Investigation.

Declaration of competing interest

The authors declare that they have no known competing financial interests or personal relationships that could have appeared to influence the work reported in this paper.

Data availability

Data will be made available on request.

Appendix A. Supplementary data

Supplementary material related to this article can be found online at https://doi.org/10.1016/j.physb.2022.414226.

References

[1] L. Soderholm, K. Zhang, D.G. Hinks, M.A. Beno, J.D. Jorgensen, C.U. Segre, I.K. Schuller, Nature 328 (1987) 604.

[2] N. Seiji, S. Adachi, H. Yamauchi, Physica C 227 (1994) 377.

[3] Y. Yamada, S. Horii, N. Yamada, Z. Guo, Y. Kodama, K. Kawamoto, U. Mizutani, I. Hirabayashi, Physica C 231 (1994) 131.

[4] N.E. Hussey, M.N. McBrien, L. Balicas, S. Horii, H. Ikuta, Phys. Rev. Lett. 89 (2002) 086601-1-4.

[5] Xiaofeng Xu, A.I. Coldea, A. Enayati-Rad, A. Narduzzo, S. Horii, N.E. Hussey, Phys. Rev. B 81 (2010) 224435-1-7.

[6] T. Mizokawa, K. Nakada, C. Kim, Z.-X. Shen, T. Yoshida, A. Fujimori, S. Horii, Y. Yamada, H. Ikuta, U. Mizutani, Phys. Rev. B 65 (2002) 193101.

[7] A.F. Bangura, Xiaofeng Xu, N. Wakeham, N. Peng, S. Horii, N.E. Hussey, Sci. Rep. 3 (2013) 3261.

[8] K. Nakada, H. Ikuta, S. Horii, H. Nozaki, I. Hirabayashi, U. Mizutani, Physica C 357–360 (2001) 186–189.

[9] M. Popa, M. Kakihara, Solid State Ion. 141–142 (2001) 365.

[10] D.P. Norton, D.H. Lowndes, B.C. Sales, J.D. Budai, B.C. Chakoumakos, H.R. Kerchner, Phys. Rev. Lett. 66 (1991) 1537.

[11] D.P. Norton, D.H. Lowndes, B.C. Sales, J.D. Budai, E.C. Jones, B.C. Chakoumakos, Phys. Rev. B 49 (1994) 4182.

[12] M. Luszczek, Physica C 355 (2001) 15.

[13] G.B. Song, J.K. Liang, L.T. Yang, J.R. Chen, G.Y. Liu, H.F. Yang, G.H. Rao, Appl. Phys. A 77 (2003) 915.

[14] R. Shannon, Acta Crystallogr. A 32 (1976) 751.

[15] T. Miyake, S. Gotoh, N. Koshizuka, S. Tanaka, Nature 341 (1989) 41.

[16] S. Funaki, Y. Yamada, F. Nakayama, J. Phys. : Conf. Ser. 507 (2014) 012016.

[17] Y. Miyachi, S. Funaki, Y. Yamada, Japan. J. Appl. Phys. 58 (2019) 070906.

[18] A. Imigi, T. Kawamata, T. Noji, M. Kato, J. Phys. : Conf. Ser. 1975 (2021) 012006.

[19] L.A. Chick, L.R. Pederson, G.D. Maupin, J.L. Bates, L/E. Thomas, G.J. Exarhos, Mater. Lett. 10 (1990) 6–12.

[20] A. Sutka, G. Mezinskis, Front. Mater. Sci. 6 (2012) 128–141.

[21] K. Koyama, A. Junod, T. Graf, G. Triscone, J. Muller, Physica C 185 (1991) 66–70.

[22] M. Hagiwara, T. Shima, T. Sugano, K. Koyama, M. Matsuura, Physica C 445-448 (2006) 111–114.

[23] K. Honnami, M. Matsukawa, T. Senzaki, H. Taniguchi, K. Takahashi, T. Sasaki, M. Hagiwara, Physica C 585 (2021) 1353869.

[24] M. Kawachi, N. Sato, E. Suzuki, S. Ogawa, K. Noto, M. Yoshizawa, Physica C 357–360 (2001) 1023–1026.

[25] R. Resel, E. Gratz, A.T. Burko, T. Nakama, M. Higa, K. Yagasaki, Rev. Sci. Instrum. 67 (1996) 1970, 1996.

[26] I. Terasaki, N. Seiji, H. Yamauchi, Phys. Rev. B 54 (1996) 11993.

[27] S. Horii, H. Takagi, H. Ikuta, N.E. Hussey, I. Hirabayashi, U. Mizutani, Phys. Rev. B 66 (2002) 054530.

[28] H.D. Yang, J.Y. Lin, S.S. Weng, C.W. Lin, H.L. Tsay, Y.C. Chen. T. H. Meen, T.I. Hsu, H.C. Ku, Phys. Rev. B 56 (1997) 14180.

[29] A. Matsuda, K. Kinoshita, T. Ishii, H. Shibata, T. Watanabe, T. Yamada, Phys. Rev. B 38 (1988) 2910.

[30] S. Horii, Y. Yamada, H. Ikuta, N. Yamada, Y. Kodama, S. Katano, Y. Funahashi, S. Morii, A. Matsushita, T. Matsumoto, I. Hirabayashi, U. Mizutani, Physica C 302 (1998) 10.

[31] Y. Yamada, A. Matsushitai, Physica C 426–431 (2005) 213.

[32] M.E. Lopez-Morales, D. Rios-Jara, J. Taguena, R. Escudero, S. La Placa, A. Bezinge, V.Y. Lee, E.M. Engler, P.M. Grant, Phys. Rev. B 41 (1990) 6655.

[33] S. Funaki, http://nsg-zaidan.or.jp/presentation/2017/pdf/4funaki.pdf.

[34] P.M. Chaikin, G. Beni, Phys. Rev. B 13 (1976) 647.

[35] M. Uchida, K. Oishi, M. Matsuo, W. Koshibae, Y. Onose, M. Mori, J. Fujioka, S. Miyasaka, S. Maekawa, Y. Tokura, Phys. Rev. B 83 (2011) 165127.

[36] T. Chiba, M. Matsukawa, J. Tada, S. Kobayashi, M. Hagiwara, T. Miyazaki, K. Sano, Y. Ono, T. Sasaki, J. Echigoya, J. Phys. Soc. Japan 82 (2013) 074706.

[37] T. Habaguchi, Y. Ono, H.Y. Du Gh, K. Sano, Y. Yamada, J. Phys. Soc. Japan 80 (2011) 02470.

[38] A. Narduzzo, A. Enayati-Rad, S. Horii, N.E. Hussey, Phys. Rev. Lett. 98 (2007) 146601-1-4.

[39] J.M. Ziman, Principles of the Theory of Solids, Cambridge University Press, 1972, Chapter 7.

[40] According to the general transport equations, the Seebeck coefficient is expressed in terms of the ratio of Peltier conductivity (σ_P) to electrical conductivity (σ), i.e., $S = \sigma_P/\sigma$. For two types of carrier, we have $\sigma_P = \sigma_1 S_1 + \sigma_2 S_2$ and $\sigma = \sigma_1 + \sigma_2$, leading to the Eq. (2).